Experimental, Numerical and Analytical Characterization of Slosh Dynamics Applied to In-Space Propellant Storage, Management and Transfer

Jedediah M. Storey[1], Dr. Daniel Kirk[2], and Dr. Hector Gutierrez[3]
Florida Institute of Technology, Melbourne, FL, 32901

Brandon Marsell[4] and Paul Schallhorn[5]
NASA KSC, FL, 32899

Experimental and numerical results are presented from a new cryogenic fluid slosh program at the Florida Institute of Technology (FIT). Water and cryogenic liquid nitrogen are used in various ground-based tests with an approximatley 30 cm diameter spherical tank to characterize damping, slosh mode frequencies, and slosh forces. The experimental results are compared to a computational fluid dynamics (CFD) model for validation. An analytical model is constructed from prior work for comparison. Good agreement is seen between experimental, numerical, and analytical results.

Nomenclature

D	=	tank diameter [m]
R	=	tank radius [m]
D_n ,E_n	=	coefficients for slosh force calculations
F_S	=	slosh forces [N]
g	=	gravitational constant [m/s^2]
h	=	fill height [m]
h/R	=	fill fraction
m	=	azimuthal wave number
m_l	=	mass of fluid [kg]
n	=	mode number; or cycle number
x	=	excitation direction
X_0	=	excitation amplitude [m]
X_0/D	=	nondimensional excitation amplitude
y	=	vertical direction
α	=	ratio of ullage-liquid interface radius to tank radius
γ	=	frequency [rad/s]
δ	=	logarithmic decrement
η	=	wall height [m]
λ	=	$\omega^2 R/g$; square of the nondimensional frequency parameter
ρ_l	=	density of fluid [kg/m^3]
υ	=	kinematic viscosity [m^2/s]
ω	=	damping factor
Ω	=	excitation frequency [rad/s]

[1] Graduate Student, Mechanical and Aerospace Department, AIAA Student Member
[2] Professor, Mechanical and Aerospace Department, AIAA Sr. Member
[3] Professor, Mechanical and Aerospace Department, AIAA Sr. Member
[4] Fluids/CFD Engineer, Launch Services Program, NASA Kennedy Space Center, AIAA Member
[5] Chief, Launch Services Program, NASA Kennedy Space Center, VA-H3, AIAA Sr. Member

I. Introduction

ADVANCEMENTS in long term, in-space, cryogenic propellant storage and transfer science and technologies are key to increasing safety, decreasing cost, and increasing payload mass of NASA's space missions. The effects of propellant slosh on spacecraft are of increasing concern. Since propellant usually makes up a large portion of a spacecraft's mass, predicting and controlling the motion of it is important. CFD tools are critical to predicting slosh dynamics and finding ways to mitigate these concerns. CFD programs are complex and require extensive experimental validation before the results can be trusted. Many CFD programs have been validated by slosh experiments using various fluids, but cryogenic fluid slosh validation experimental data is lacking.

The initial results of an extensive slosh testing program at the FIT Aerospace Systems And Propulsion (ASAP) laboratory are presented in this paper. The research is supported by a NASA Space Technology and Research Fellowship (NSTRF) and the KSC Launch Services Program (LSP). The project over the past year focused on performing ground based slosh experiments in order to gather data relevant to validating CFD simulation tools for predicting slosh dynamics. Specifically, an approximately 30 cm diameter spherical aluminum tank was used to perform forced sinusoidal and damping slosh experiments with water and liquid nitrogen (LN2). Water tests are used for experiment validation purposes. Select cases from the experiments were simulated using STAR-CCM+® [1].

The paper begins with a discussion of analytical models. The section that follows details the experimental setups, testing, and data post-processing. Next, the numerical methods used for simulating fluid slosh are presented. A discussion and comparisons of the analytical, experimental, and numerical results follows. Conclusions from these results are discussed next. Finally, extensive future work, including test improvements, new ground experiments, a microgravity test platform, and new simulations, is discussed.

II. Analytical

Analytical slosh models for rigid spherical tanks based on the works summarized in Ref. 2 were developed to guide the experiment design and for comparison purposes. Analytical asymmetric and symmetric modes are presented, and despite the non-parallel wall nature of spherical tanks, an analytical solution to the inviscid fluid equations for lateral, forced, linear sloshing exists and is presented here.

Calculating the modes of a spherical tank is complicated[2]. The final equations require extensive numerical integration and the evaluation of the resulting matrix eigenvalue problem; no attempt was made to evaluate these equations. Instead, the first three modes of the m=0,1 azimuthal wave numbers (corresponding to symmetric and antisymmetric respectively if the tank was cylindrical) natural frequencies versus fill fraction curves are extracted and tabularized from Fig. 1.12 of Ref. 2 and Table 2 and Fig. 3 of Ref. 3. While this introduces some error, it saves computation time.

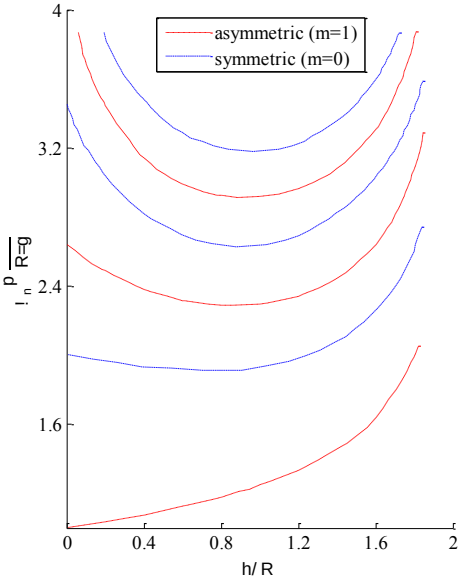

Figure 1. Frequency vs. Fill Fraction for First Three Modes.

Figure 1 depicts the extracted nondimensional frequency vs. fill fraction curves. Linear interpolation is used to calculate the expected natural frequencies of the modes for a given fill fraction. These tables are also used in the calculation of the analytical slosh forces.

Ref. 2 presents Ref. 4's analytical formulation for the determination of slosh forces in spherical containers under lateral excitation. The final resulting differential equations are as follows:

$$\frac{d^2\eta_n}{dt^2} + {\omega_n}^2\eta_n = -{\lambda_n}^2\alpha\frac{D_n}{E_n}\frac{d^2x}{dt^2} \qquad (1)$$

$$F_s = -m_l\frac{d^2x}{dt^2} - \pi\rho_l(\alpha R)^2\sum_{n=1}^{\infty} D_n\frac{d^2\eta_n}{dt^2} \qquad (2)$$

, where η is the wave height at the wall and F_s is the slosh force. D_n and E_n are calculated from integrals of eigenfunctions of the kernel function. No attempt was made to calculated these coefficients; instead, they were tabularized from Fig. 2.21 of Ref. 2, in a similar fashion to the natural frequencies versus fill fraction curves and for similar reasons.

All equations are entered, and tables imported, into MATLAB® [5]. For a given amplitude, excitation frequency, and fill fraction, Eq. (1) is solved for the first three asymmetric modes (m=1) using the ODE45

solver. The required natural frequencies are obtained by interpolation of the nondimensional frequency versus fill fraction tables. Contributions from other azimuthal wave numbers and higher modes are not considered. The contributions of the first three modes are summed, and the resulting wall wave height and force versus time curves are computed.

Two common nondimensional parameters are the the slosh force parameter $F_{max}/(\rho_l g D^2 X_0)$, where F_{max} is the maximum F_s for a given frequency, amplitude, and fill fraction, and excitation frequency parameter $\Omega\sqrt{R/g}$. A slosh force parameter versus excitation frequency parameter curve is computed by looping through the aforementioned process numerous times over a range of frequencies. To decrease computation time, the internal loop that contains the ODE45 function is computed in parallel. An example plot for 50% fill fraction in the tank considered is shown in Figure 2.

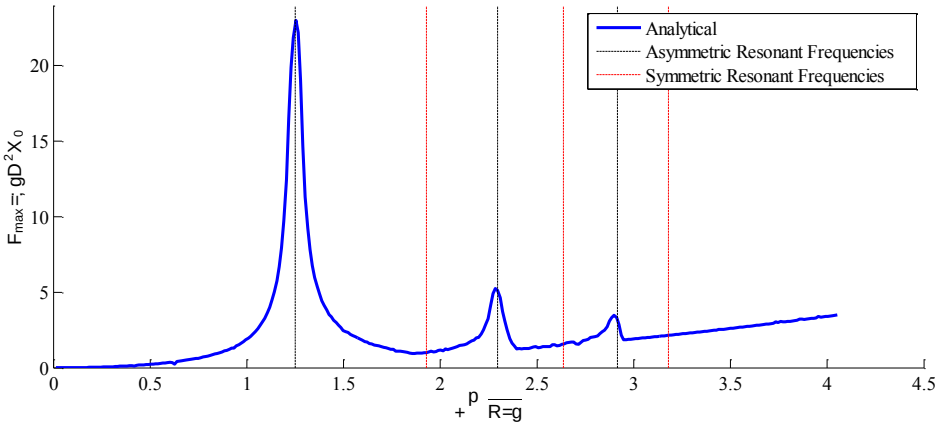

Figure 2. Force Parameter vs. Exciation Frequency Parameter Example.

As can be seen in Figure 2, the plots created with this method are imperfect: the resonance peaks are not asymptotic and the curves are not smooth, particularly at higher frequencies. Evaluating at discrete frequencies, table interpolations, and only including the influences of the first three modes are likely the cause of these imperfections. The error introduced by these simplifications has not been quantified, but it is assumed to be small.

III. Experimental

The following sections discuss the experimental setups, instrumentation, software, tests performed, and problems encountered.

A. Experimental Hardware

Two similar experimental setups were utilized for the experimental portion of this project, one for the damping tests and one for the forced sinusoidal tests. Common to both setups are the tank and tank frame, so these are presented first, and then the overall setups are presented.

1. *Tank*

Properties of the tank used for testing are summarized in Table 1.

Table 1. Tank Properties

Material	3003 Aluminum
Inner radius	0.148 m
Wall thickness	3.175 mm
Flange material	T6-6061 Aluminum
Flange diameter	0.356 m
Flange thickness	6.3 mm (each)
O-ring diameter	3/32 in

A flanged design was chosen to allow for easy disassembly for cleaning and flexibility for future testing, e.g. adding baffles or additional tank sections. The tank was fabricated from two COTS hydroformed domes. The inside of the tank was sanded with sandpaper up to 1500 grit to remove shallow surface defects and discoloration. The tank was not polished because doing so might have resulted in too much light being reflected back into the top-mounted camera. Flanges were machined and welded to the domes. A ball endmill was used to cut an O-ring groove in one of the flanges. O-ring cord stock is used for water testing.

While Indium is ideal for cryogenic seals, it is expensive. Instead, Lead wire is used for LN2 testing. Since Indium and Lead have similar low-temperature properties, it is hypothesized that Lead works just as well as Indium for non-pressurized cryogenic seals. The fact that no leaks have been observed during LN2 testing support this hypothesis.

A hole was cut in the top of the tank to allow for a camera and lighting. An aluminum ruler was machined down and screwed to the inside wall of the tank along the forcing axis for measurement of fluid wall height. Seven brass thermoprobe pass-throughs were mounted in the tank wall along the ruler at various locations (see Section III.B.2). PTFE thread sealant tape prevented leaks from threaded holes.

The design of the tank mounting brackets was considered a high priority because a failure of one of these would be catastrophic in terms of safety and experiment damage. The requirements for the tank mounting brackets include: low thermal conductivity, high strength at cryogenic temperatures, stiffness, and resistance to thermal cycle fatigue. Various materials were considered, but ultimately polycarbonate was chosen. FEA analyses were performed with room temperature properties to guide the design. Finally, four tank mounting brackets were machined out of 0.25 in thick polycarbonate sheet. No cracks in the brackets have been observed.

Various types of insulation were considered. Requirements for the insulation included: low thermal conductivity, ability to withstand cryogenic temperatures, easy to handle, and manufacturability. Although commonly used in space propulsion applications, Multi-Layer Insulation (MLI) was rejected because it is very expensive and best suited for vacuum conditions. Aerogel blanket insulation was also considered. While significantly less expensive than MLI, it was ultimately rejected because of cost. Insulation domes were machined from large blocks of 2 lb/cu.ft. density polyurethane foam. The outer surface of the insulation domes was covered in aluminized nylon "space blanket" material to decrease radiative heat transfer.

Various problems with the tank occurred during fabrication and testing that result in some uncertainty. The domes are not perfectly spherical. The radius varies by approximately +/-1 mm and thickness varies by about +/- 0.1 mm. Some minor warping occurred during welding of the flanges to the domes, but by aligning the warps in the two halves, the potential problems were mitigated. The welding also slightly deformed an approximately 15mm wide ring around the middle of the tank, turning it into a flat cylindrical section. Galvanic corrosion was observed around the brass thermocouples; the PTFE thread sealant helped mitigate this, but it is still present. Shallow corrosion pits form in the aluminum after extended (8+ hour) exposure to tap water. The corrosion products have to be cleaned off between water tests. The inner radius of the insulation was machined too small, resulting in a gap in the insulation. A gap had to be cut into the insulation to allow assembly of the insulation around the tank's thermocouples. All gaps are filled with pieces of foam covered with metallic tape before testing. Condensation and ice formation around these regions are indicative of significant heat leaks in those areas.

2. *Frame*

The tank frame was based of the designs of Ref. 6 and fabricated out of T-slot aluminum extrusions. The main requirement for the tank frame is stiffness to prevent mechanical vibrations. A secondary requirement is low mass to maximize the excitation capabilities of the linear stages. The frame was designed to allow for the easy addition of a pitching rotational axis, similar to the one presented in Ref. 6.

3. *Damping Test Experimental Setup*

A linear stage in the Mechatronics Lab at FIT was used to perform damping tests. This stage has a belt-driven carriage that can be attached to a stage mounted on roller bearings and linear rails. The total useable travel is approximately 1.5 m, though no more than 6 cm was used for this project. A servomotor with encoder feedback drives the belt. Figure 3 is a picture of the tank, tank frame, linear stage, and instrumentation.

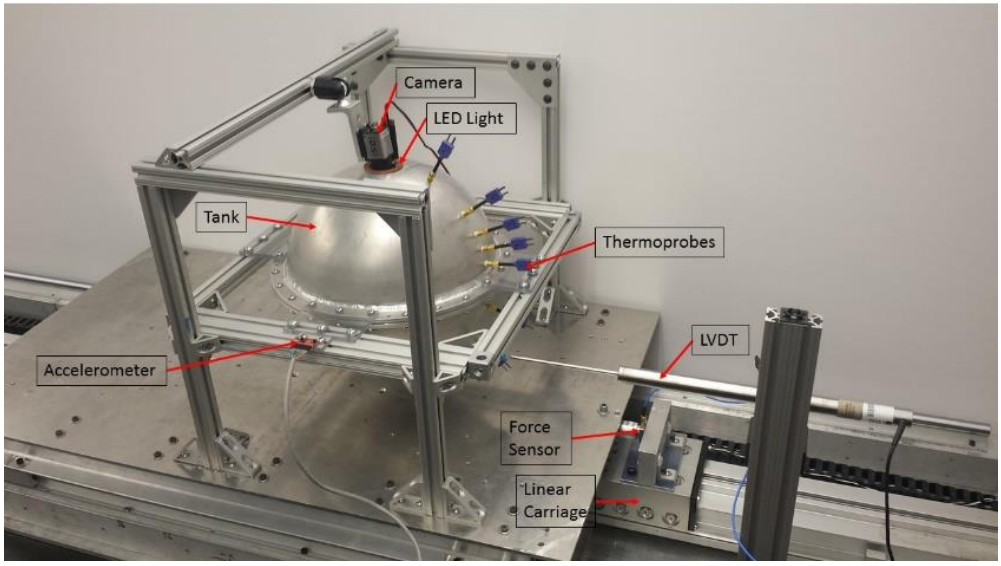

Figure 3. Damping Test Setup. *Tank pictured without insulation.*

This stage is capable of high amplitude, high force loading of propellant tanks and has been used in many prior FIT slosh testing projects. However, interactions between non-linear kinetic and static rail friction, belt stretching, and the belt sprockets result in low frequency, high amplitude mechanical vibrations on the order of the slosh forces trying to be measured. Therefore, accurate force data could not be collected when the stage was in motion. Since damping calculations simply require static data collection after an initial excitation, this stage was useful for those tests.

4. *Forced Excitation Test Experimental Setup*

The mechanical vibration problems with the linear stage mentioned in the previous section prevented its use for forced sinusoidal testing. As a result, a novel approach for performing forced and free multi-DOF slosh testing was developed. A picture of the 1 DOF forced sinusoidal testing setup is presented in Figure 4.

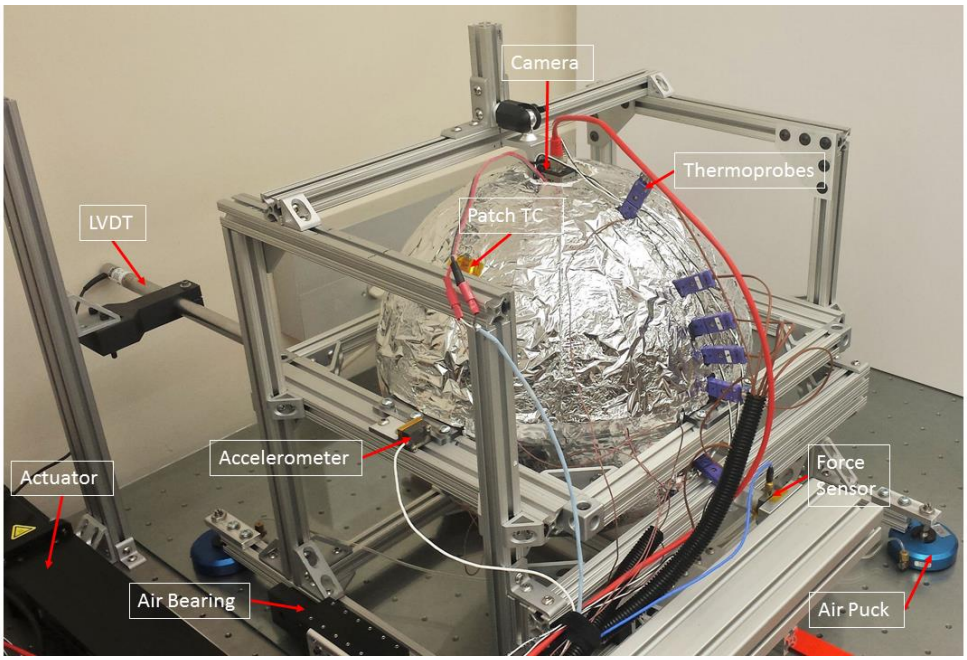

Figure 4. Forced Excitation Setup.

A lead screw-based linear actuator eliminates the problems seen with the belt actuator in the other stage. Instead of rails, graphite air pucks are used to float the tank and tank frame a few microns above the surface of a glass sheet,

effectively mitigating both static and kinetic friction. An air bearing is used to restrict motion to one linear DOF. A floating sub-frame was constructed out of T-slot aluminum extrusion to hold the air pucks and tank frame. An extra structural beam (the "force beam") had to be added to the tank frame to align the force sensor axis through the average CG location of the floating subsystem. A cantilevered beam (the "arm") extends out from the lead-screw actuator to hold the force sensor. The resonant frequencies of a simple mass-spring system for both beams was calculated to ensure that they were stiff enough to prevent resonance. Every attempt was made to enforce square-ness and level-ness.

The table that the test setup is mounted to is a self-leveling optics-bench style. However, it was discovered that the lateral stiffness of these tables is low when they are floating, necessitating the depressurization of the self-leveling bellows and manual shimming the table to level within 1 degree. A strap was added around the table to increase lateral stiffness, but the table still oscillates with an amplitude of a few mm during high force tests, creating a non-inertial reference frame. The accelerations resulting from the table motion were neglected in all analyses.

Despite the attempts to stiffen the system, a roughly 25 Hz translation mechanical resonance mode exists due to an unknown interaction between the cantilevered arm, force sensor, and force beam. Under normal test conditions, this vibration is low amplitude (< 0.1mm, < 10N) and was simply filtered out (see Section III.D).

All future slosh testing will be conducted on this table. The advantages and potential uses of this "floating tank" approach are discussed in Section VI.

B. Instrumentation

The instrumentation system includes a data acquisition system, sensors, and camera.

1. *Data Acquisition System*

The data acquisition system consists of a National Instruments (NI) PXI chassis, NI motion controller, two NI E-series data acquisition (DAQ) cards, two instrument interface boards, and a PC running LabVIEW 2012. All sensors outputs are read by that system. One DAQ card has 12 bit analog-to-digital converters (ADCs) and the other 16 bit ADCs for the analog channels. The majority of the thermocouples are connected to the 12 bit card, while the other sensors are connected to the 16 bit card. The motion controller card is only used to control the belt-driven linear stage. A separate computer runs the motion control software that interfaces with the motion controller for the lead-screw actuator. For both test setups, that computer also runs the camera frame-grabbing code. This was done to prevent CPU overload on the LabVIEW computer. Frame capture is synchronized with the data collection via a hardware trigger pin that is pulsed from a digital output from one of the DAQ cards.

The DAQ cards are synchronized via a digital start trigger and their sample clocks. The system was tested with sample rates of up to 6 kHz, though the forced sinusoidal and damping data were gathered at 2 kHz and 1 kHz respectively.

2. *Sensors*

An accelerometer aligned with the forcing axis. It is calibrated using earth gravity as a reference. A triaxial piezoelectric PCB force sensor collects force data along the forcing axis; the other two axes are unused because movement is restrained in those directions. The force sensor is preloaded as per the manual. Calibration was checked, and the published conversion factor was determined to be acceptable. Piezoelectric force sensors are good for measuring alternating forces but poor at measuring constant forces due to discharge; this causes the sensor offset to drift in a non-linear fashion. Special care had to be taken when analyzing the force data to correct for these drifts (see Section III.D). A DC linear variable differential transformer (LVDT) with four inches of travel is used for position measurement. It was calibrated with dial calipers. All angular alignments of these sensors is within 1 degree. See Figure 4 for sensor locations.

All avenues for noise reduction were investigated. All sensors are grounded, and the sensors' grounds are isolated from the motor controllers' grounds. The LVDT, accelerometer, and force sensor have electrical noise bands of about 0.2 mm, 0.2 m/s^2, and 1 N respectively. Lowpass filtering produces significantly better precision. Despite this, the signal-to-noise ratio for the accelerometer is borderline too low for lowest amplitude motion cases. The accelerometer also experienced 5-10 s periods of high-amplitude, low frequency noise during a few tests; the cause of these "glitches" is unknown.

The number of thermocouples was determined by the number of remaining analog input channels of the data acquisition system. Seven 1/16 in, grounded junction, stainless steel, E-type thermoprobes penetrate the tank wall with their tips approximately 1.5 mm inside the inner wall. Positions correspond to various volumetric fill fractions (see Figure 5). A carbon fiber tube between the pass-through and the thermoprobe connector stiffens each probe. Four additional, adhesive-patch-type thermocouples are placed outside the tank. Two are adhered directly to the tank wall

as seen in Figure 5. Two more (one is pictured in Figure 4) are located on the outside of the insulation at the same elevations, but rotated 90 degrees so that they are not adhered over the insulation gap (see Section III.A.1).

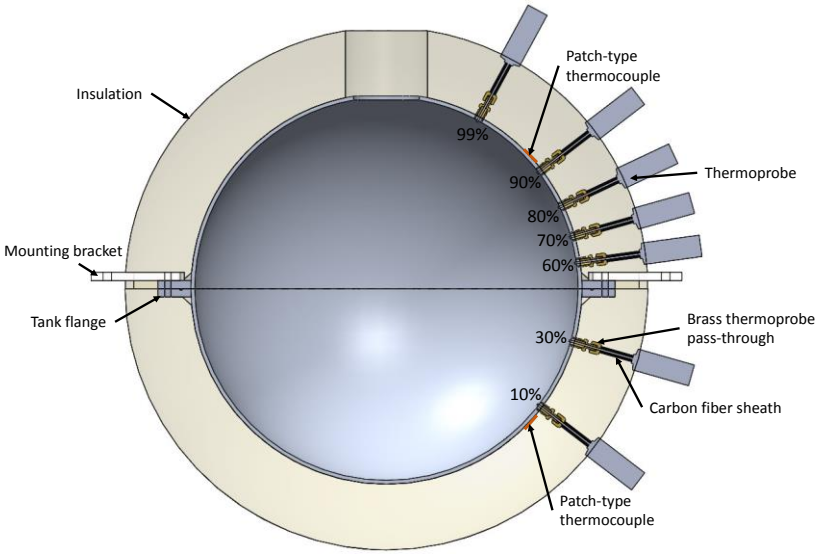

Figure 5. Tank CAD Cross-section.

Unfortunately, the NI thermocouple modules being used, which handle cold junction compensation and amplification, are over 10 years old and out of spec. When subjected to the same temperature, each thermocouple reads a significantly different temperature: 5 °C and 20 °C maximum differences for room and LN2 temperatures respectively. Attempts to zero the modules failed. Static temperature data was collected for both room temperature and LN2 temperatures for corrections to be attempted during post-processiong.

3. *Imaging*

A 5 MP IDS® ethernet machine vision camera was mounted above the tank to capture images of the fluid surface (see Figure 3). The camera was controlled via a custom C code that grabs frames from the camera when it detects a pulse on its hardware trigger pin. The maximum frame rate achieved was 34 fps at approximately 1 MP resolution. Frame rate was limited by the ethernet bandwidth.

Imaging inside of a small opaque tank was challenging. Small slosh tanks are typically made transparent[6] to allow the placement of cameras and lighting far enough away to capture images of the fluid surface without the use of distorting wide angle lenses. However, metallic tanks are required for cryogenic fluid slosh testing, which restricts the camera location to the ullage. Small opaque tanks, like the one used for this project, require a lens with a large field of view in order to see the entire inside of the tank. Thus, a fisheye lens was used for all tests. An image rectifying script was written in MATLAB to attempt to correct for the distortion caused by the fisheye lens. It did not seem to reduce distortion significantly, so all pictures of the inside of the tank that appear in this paper are uncorrected. Lens icing during LN2 tests turned out to be a non-issue because the flow rate through the tank opening due to boil off was enough to prevent water vapor from entering the tank and condensing on the lens.

An additional difficulty with opaque tanks is lighting. The brightness of the light is inversely proportional to the frame exposure time, which directly influences motion blur. Thus, a brighter light will result in less motion blurring. Besides brightness, other requirements for the lighting include: low heat production, wavelength(s) near the highest sensitivity wavelengths of the camera, and ability to withstand cryogenic temperatures. White LEDs were selected because the meet all of these criteria. LEDs can operate submersed in LN2, though their wavelengths shift shorter because the bandgap voltage increases, which gives a green hue to all of the LN2 test pictures. Ten 3 W LEDs were assembled into a ring light for the camera, which was driven by a constant current power supply. The maximum operating power achieved by the ring light with and without LN2 cooling was about 2.5 W and 6 W respectively. As testing progressed, it was discovered that, while LEDs could be operated continuously at LN2 temperatures, thermal cycling between room temperature and LN2 temperature breaks them. The LEDs will be replaced with a fiber optic light source for future testing.

4. *Fluid Height Measurement*

A thin metric ruler with 1 mm, 5 mm, and 10 mm markings is mounted to the inside wall of the tank to allow for fluid height measurements. A spreadsheet program and MATLAB script were created to convert between volume, vertical wall height (fill height), and arc length wall height (ruler measurements). The location accuracy of the ruler was checked using a graduated cylinder and water, and found to be as accurate as the graduated cylinder could measure. During post-processing, camera frames are stepped through and fluid height readings at maxima and minima are taken. Because resolution was sacrificed for a higher frame rate, the 1 mm lines are indistinguishable. The 5 mm markings are distinguishable, making the measurement error +/- 2.5 mm. There is also a smaller error introduced from having discrete frames, and therefore missing exact maximum or minimum heights. The dominant error for LN2 tests comes from boiling. Higher fill levels exhibited more boiling than lower fill levels; estimated measurement errors range from +/- 5 mm to +/- 3 mm. Since the tank is spherical, the conversion from arc length error to volume error is not constant, but can be calculated as a function of fill height.

C. Software

A LabVIEW[7] Virtual Instrument (VI) program is implemented for the data acquisition system for both test setups. All channels are synchronized using digital start triggers and their sample clocks. Data collection is handled by the DAQ cards, with data transfers happening incrementally, allowing for sample rates above the software-timed limit of 1 kHz. A proportional-integral-derivative (PID) motion control code is added to the VI for the belt-driven linear stage setup; this code uses a NI PXI motion card to read the encoder signals and output commands to the motor controller. The PID controller was tuned for linear stage system. A Beckhoff combined programmable logic controller (PLC) and motor power supply came with the lead-screw actuator's motor. The PLC is programmed using TwinCAT3® [8]. The motion controller is not a simple PID. Luckily, the default values produced acceptable performance, though tuning the controller would likely yield better results.

D. Test Procedures and Matrices

Two main types of tests were performed: damping and sinusoidal excitation. Static boil-off tests were also performed.

Plain tap water was used for water tests, and volume measurements were made with a graduated cylinder and checked with the ruler on the inside of the tank. A chill-down process was used for LN2 tests to prevent thermal shock. Small amounts of LN2 were poured into the tank and allowed to boil off, after which the tank was filled and allowed to sit for 30 min. LN2 fill level was measured with the ruler on the inside of the tank. LN2 was periodically refilled as needed.

1. *Damping Tests*

Damping tests were performed for water at 10 different volume fractions. Each volume fraction was excited with sinusoidal motion on the damping test setup at two frequency/amplitude combinations. The frequencies used were 1 Hz and 2 Hz, but the amplitudes were varied to ensure enough excitation and prevent fluid from splashing out of the tank. After two cycles of excitation, the motion was stopped and data was recorded for 30-120s, depending on how long the force took to decay. Each of these tests was performed twice, for a total of four damping tests per water volume fraction.

Tests for LN2 were similar, except the boil off made obtaining precise volume fractions difficult. The same total number of tests were performed, but spread over more volume fractions. Each LN2 volume fraction had at least one 1 Hz and one 2 Hz test.

Data post-processing was done in MATLAB. Position and acceleration data were ignored for damping rate tests. The excitation cycles were trimmed from the force data. Most of the tests' force data exhibited an exponential decay (see Section III.B.2) and drift. An exponential fit was subtracted from the force data in an attempt to detrend it, though the drift still remained. The force data was then filtered using MATLAB's non-casual "filtfilt" command with a 7th order Chebyshev Type-II IIR filter with a -50 dB gain at a 15 Hz cut-off frequency. The aforementioned drift necessitated the calculation of the logarithmic decrement (see Section V.B) with the valley-to-peak force amplitude decay and not simply the maximum force decay. Wave amplitude maxima and minima were read by eye using the captured images of the internal ruler.

Damping results and comparisons to CFD and previous work results are presented in Section V.B.

.

2. *Forced Excitation Tests*

A forced sinusoidal excitation test consists of filling the tank to a specific volume fraction and running approximately 20 frequency/amplitude combinations for 30-60s each, depending on frequency. Nine volume fractions

were planned and each test was to be repeated twice. Unfortunately, time constraints resulted in only two complete volume fractions, 20% and 50%, for water with repeats and one complete volume fraction, 50%, for LN2 with a partial set of repeats, all totaling to about 150 forced excitation tests.

Frequencies were dependent on the fill fraction. The tank was excited at the theoretical first, second, and third asymmetric and symmetric mode frequencies for the 50% water and LN2 cases, with various other frequencies spaced between these. The 20% water case was excited near the first asymmetric mode and various other frequencies spaced between 0.5 Hz and 4.5 Hz. The exact theoretical higher mode frequencies were not used. Amplitudes were chosen to ensure enough excitation and prevent fluid from splashing out of the tank; this was typically near 3 mm, though it was higher for very low frequencies and lower for the first asymmetric mode resonant frequency.

Images could not be captured for the LN2 forced excitation tests. The LED light ring (see Section III.B.3) failed due to thermal cycling, and time constraints prevented continuous LED replacement. Fluid height during filling and replenishing was measured using a USB snake camera instead of the IDS camera.

Post-processing for the forced sinusoidal data was more complicated than the damping data. Position and acceleration data were not ignored. Acceleration was detrended with the MATLAB "detrend" function, which subtracts a linear best fit. Position needed to be offset. Scaling was done in the LabVIEW data collection program, so no additional scaling was done. The position and acceleration data were filtered using MATLAB's non-casual "filtfilt" command with a 7th order Chebyshev Type-II IIR filter with a -50 dB gain at a 15 Hz cut-off frequency. A best fit sinusoidal waveform was fit to the filtered position data to determine the actual amplitude for input into the CFD. The maximum deviation from commanded amplitude was +6%, i.e. the actual amplitude was about 6% higher than the commanded amplitude, which occurred for the lowest amplitude case. Average deviation from commanded amplitude was about +1%. The filtered position data was differentiated using the second order central difference formula and compared to the filtered acceleration data and the ideal sinusoidal acceleration waveform derived from the position-fit waveform to check for motion anomalies.

Since the tank was constantly in motion, the force data collected included the inertia of the tank and frame and any friction acting on them. These forces had to be subtracted from the total (measured) forces to derive the slosh forces. Empty tank tests at all frequency/amplitude combinations were performed. The force data from each test was detrended with an exponential fit and filtered using a similar filter to the one used on the position and acceleration data. The empty tank force data was then split up by cycle and averaged to form an average force cycle. This was loaded into the main post-processing script and assembled into a waveform of length equal to the length of the total force data. The total force data was detrended with an exponential fit and filtered using the same filter used for the position and acceleration data. The empty force waveform was then subtracted from the total force waveform to form the slosh force waveform. This method is preferable to subtracting structural mass times acceleration from the total forces because it only relies on one sensor instead of three (scale and accelerometer are the additional two), and it corrects for frictional forces. The force data from the forced sinusoidal tests did not exhibit the drift seen in the damping tests.

Forced sinusoidal excitation results and comparisons to CFD, analytical, and previous work results are presented in Section V.C.

E. Uncertainty

Many sources of error have been discussed in the previous sections. A few more are mentioned here.

About halfway through the testing program, the graduated cylinder used for the water tests volume was checked with a scale and other graduated cylinders. It turns out that its 1 L mark corresponds to about 975 mL, which results in about -330 mL of volume error for a nearly full tank. This was corrected for the 50% water forced sinusoidal testing, but all water damping tests and the 20% forced sinusoid test had volumes 2-3% too low. This error has *not* been accounted for in data processing.

Before the tank material was decided, shrinkage of the aluminum tank's radius at LN2 temperature was estimated to be about 1 mm. Observations of the movement of the tank's brackets, the screws for which are not fully tightened to the frame until after chill-down, validates this estimate. No corrections have been made for this change in volume.

Volume measurement is likely the biggest source of error for both LN2 and water tests. The ruler measurement errors for both water and LN2 are mentioned in Section III.B.4. For water volume, the graduated cylinder error was mentioned earlier. For LN2, the volume error comes from measurements based on the internal ruler. The maximum volume error will be near the 50% fill line because the volume changes the most with arc length at this location for a sphere. The ruler measurement error is about +/- 4 mm at 50% fill. Thus, the maximum volume error due to ruler measurement is about +/- 270 mL, which is about +/- 2%.

Although tests were repeated as many times as time allowed, no rigorous uncertainty analysis has been performed yet due to time restrictions.

IV. Numerical

CFD simulations were performed using STAR-CCM+ on a NASA computer with dual, 8 core Intel Xeon 3.1 GHz processors and 64 GB of ram.

The tank was modeled as a perfect sphere with a ring-shaped pressure outlet that represents the gap between the camera lens and the wall of the hole in the tank. The following settings were used for all simulations: implicit unsteady with 2nd order accurate time formulation, muliphase segregated volume-of-fluid (VOF), laminar. Volume fraction was initialized with a field function. An isosurface derived part defined the water-air surface. Solution history was saved every 0.025 s to allow for the creation of smooth surface animations. Three axis forces and moments were exported every time step. A field function was written to emulate the tank's internal ruler to measure fluid wall height as a function of time.

Position-based movement was implemented using a field function and user-defined vertex motion. Two field functions were tried. One imported a table of the filtered experimental position data. Tiny slope changes in the position data caused large force oscillations in the CFD. It was reasoned that the effects of the imperfections in the position profile (and the small oscillations filtered out of the experimental force data) were small. Thus, a second field function was implemented that calculated a pure sinusoidal position profile based on frequency and amplitude. For the forced sinusoidal simulations, the amplitude was corrected based on the best-fit-sine wave mentioned in Section III.D.2.

A grid and time step independence study was started. The meshes used were hexahedral dominant with a single layer of prism cells on the wall. A 1.5 Hz, 3 mm amplitude, 10 s case was used for the study. A 115k and 340k cell mesh were considered. Time steps of 0.001 s and 0.0005 s were also considered. The forces and moments were used for comparison. The results were determined to be neither time step nor mesh independent with a time step of 0.0005 s and the 340k mesh, though there was good agreement for the first 5 s. The results seemed to have a stronger dependence on mesh than time step, so a 580k cell mesh was created. That mesh and a time step of 0.001 s were used for all simulations presented in this paper with the hope that the experimental results would agree well. A runtime of 10 s with that mesh and time step on the aforementioned computer takes approximately 18 hours. Computation time was the limiting factor for cell count and time step.

CFD results are presented in the next sections.

V. Results

A. Static Boil-off

The insulated tank was filled with LN2 to about 90% following the chill-down process. Temperature data was taken at 1 Hz. Fluid level was measured with the internal ruler by eye for four, approximately 20 min periods. Table 2 summaries the results of the test.

Table 2. Static Boil-Off Test Results

Arc height start [m]	Arc height end [m]	Δ Volume [m^3]	Boil-off rate [kg/h]
0.315	0.303	0.00054	1.307
0.23	0.224	0.000412	0.997
0.165	0.157	0.000382	0.928
0.132	0.12	0.000352	0.851

The first start arc height corresponds to 86% volume fraction and the last end arc height corresponds to 7% volume fraction. The results support the qualitative observation of decreased boiling with decreased fill volume. These results, along with the corresponding temperature data, will later be used to validate a Generalized Fluid System Simulation Program (GFSSP)[9] tank model.

B. Damping

1. *Logarithmic Damping and Damping Factor*

Two parameters are commonly used to describe the damping of a tank and fluid: logarithmic decrement and damping factor. Two ways to calculate logarithmic decrement from experimental data are via force decay and wave amplitude decay.

$$\delta_F = \ln\left(\frac{F_n}{F_{n+1}}\right) \tag{3}$$

$$\delta_{WA} = ln\left(\frac{W_n}{W_{n+1}}\right) \tag{4}$$

$$\gamma = \frac{\delta}{2\pi} \tag{5}$$

F_n is the force of cycle n and W_n is the wave amplitude of cycle n. Few theories exist for calculating an analytical solution for damping factor[10]. Various experimental correlations for spherical tanks have been developed for logarithmic decrement based on force, wave amplitude, or for either. Note that these correlations are not equivalent and do not always agree well. The data that they are based on may have come from slosh that was linear, nonlinear, or mixed. Some of these correlations are listed below.

Correlation	Valid Range	Citation	Equation
$\delta_F = 0.131B^{0.359}$	$\frac{h}{R} = 1.0$	Ref. 10	(6)
$\delta_{WA} = 0.08347\sqrt{B}\left(\frac{R}{h}\right)$	$0.1 \le \frac{h}{R} \le 1$	Ref. 10	(7)
$\delta_{WA} = 0.08347\sqrt{B}\frac{1+0.46\left(2-\frac{h}{R}\right)}{1.46\left(2-\frac{h}{R}\right)}$	$\frac{h}{R} \ge 1$	Ref. 10	(8)
$\delta = 0.32\left(\frac{1}{G_A}\right)^{0.359}$	$\frac{h}{R} = 0.5$	Ref. 2	(9)
$\delta = 0.39\left(\frac{1}{G_A}\right)^{0.359}$	$\frac{h}{R} = 1$	Ref. 2	(10)
$\delta = 0.66\left(\frac{1}{G_A}\right)^{0.359}$	$\frac{h}{R} = 1.5$	Ref. 2	(11)

$B = \frac{10^4}{2\sqrt{2}}\frac{\nu}{\sqrt{R^3 g}}$ and $G_A = \frac{\sqrt{R^3 g}}{\nu}$. Note that Eq. (7) and Eq. (8) are equivalent to Eq. 2.9a and Eq. 2.9b of Ref. 11 respectively when the characteristic length is tank radius.

2. *Calculating Logarithmic Decrement*

Logarithmic decrement was calculated using both the force decay method and the wave amplitude decay methods. Due to the nonlinear drift from the force sensor, the valley-to-peak force was used instead of the peak force in Eq. (3). To be consistent, the CFD force-based logarithmic decrement was calculated the same way. Experimental wave amplitude was obtained from image data. CFD wave amplitude was obtained from a field function emulating the ruler inside the tank. The valley-to-peak wave amplitude was used instead of the peak wave amplitude in Eq. (4).

A maxima and minima search algorithm was written in MATLAB to find the valleys and peaks of the force and wave amplitude wave forms. A necessary input into this algorithm is the approximate frequency of the main mode of oscillation, i.e. the first asymmetric slosh mode frequency. This was calculated from the experimental and CFD data using a Fast Fourier Transform (FFT). In addition to being used for the maxima and minima search algorithm, the calculated first mode frequencies are compared to analytical predictions in Figure 6. Overlapping right-pointing triangles represent repeated experiments. For water, CFD data exists for 50% volume fraction. For LN2, CFD data exists for 50% and 70% volume fraction. The specifics of the damping simulations run are summarized in Table 3. Analytical, CFD, and experimental first mode frequencies all match well.

Table 3. Damping CFD Simulations.

Fluid	Volume Fraction %	Excitation Frequency [Hz]	Amplitude [mm]	Number of Excitation Cycles
Water	50	1	30	2
LN2	50	1	30	2
LN2	50	2	5	2
LN2	70	2	5	2

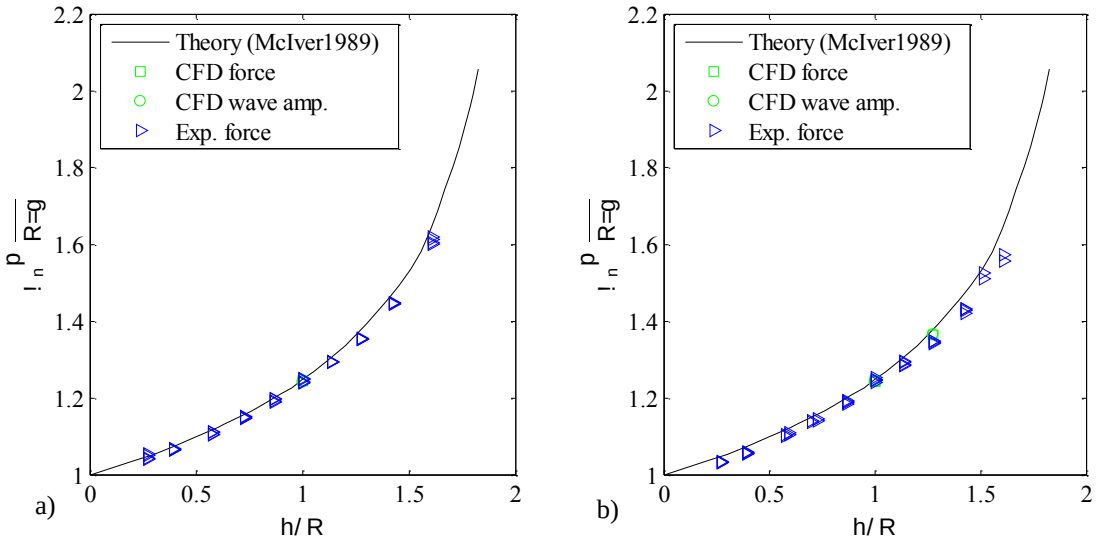

Figure 6. First Mode Frequencies for a) Water and b) LN2.

Unfortunately, the logarithmic decrement versus time results for both experimental and numerical data were noisy. Outliers greater than 1.5 times the standard deviation were discarded; this usually included the first cycle or two. The remaining results were smoothed with MATLAB's "smooth" function using the "rloess" method. A time averaged logarithmic decrement was then calculated from the smoothed results.

3. *Plots*

Figure 7 is a comparison between the correlations, Eqs. (6)-(11), and data from Refs. 12 and 13. A dependence on excitation amplitude is also apparent. For reference, the nondimensional excitation amplitudes, $\frac{X_0}{D}$, for the damping test portion of this project ranged from 0.0169 to 0.1014. Thus, the cases associated with larger excitation amplitude in Figure 7 provide a sense of the order of magnitude and variance to be expected from logarithmic decrements derived from this project's experiments.

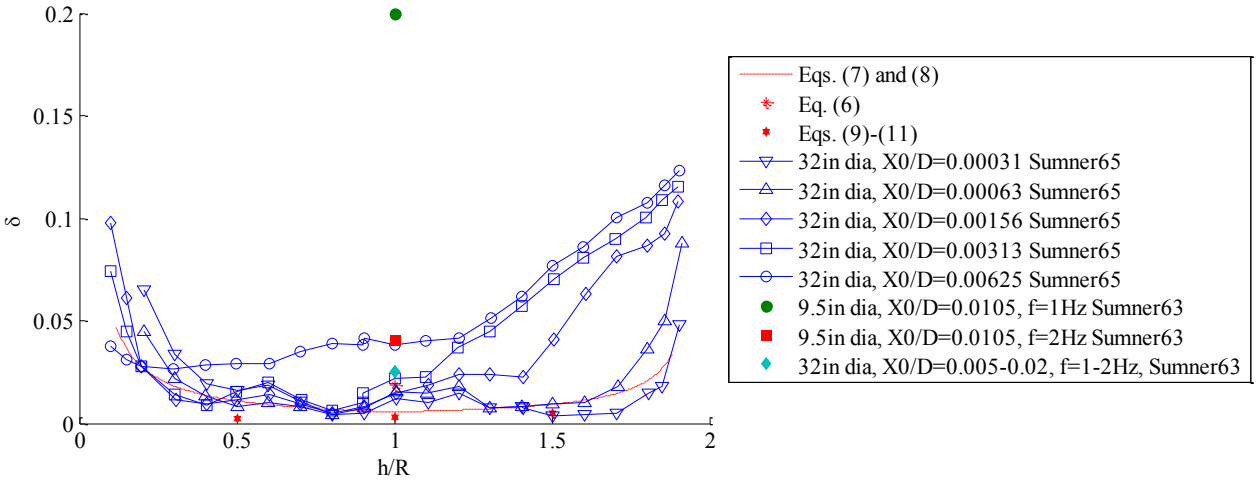

Figure 7. Correlations vs. Sumner Experimental Data. *Working fluid was water for all cases. Note that the correlations were calculated for a 32 in diameter tank with water.*

The correlations underpredict logarithmic decrement for the majority of the Figure 7 experimental results. The following discussion will regard only the largest three excitation amplitude data series. All of the correlations underpredict the results for fill fractions greater than or equal to 1, with an error of 400% or more for some points. For fill fractions less than one, the correlations usually underpredict, but sometimes overpredict, the logarithmic decrement. The curve defined by Eqs. (7) and (8) does not adequately capture the shape of the data curves for any of the results. The shape disagreement is most extreme for large amplitudes, where the logarithmic decrement is generally lower for low fill fractions and higher for high fill fractions, though the upward trends for the lowest and highest fill fractions are present in both the Eqs. (7) and (8) correlation and the data. Also note the local maxima around fill fractions of 0.6 and 1.2 for some of the data series; it is unclear what caused these. The Eqs. (9)-(11) correlations underpredict the results for all but one point, and the Eq. (6) correlation performance is mixed. Because of the large difference between the correlation and the data for the three largest excitation amplitude cases, it is highly likely that the slosh was nonlinear for fill fractions greater than 1. Given the Figure 7 results, any agreement between the experimental data for this project and the correlations will be deemed "fair" if the error is within 100%. More than 100% error will be deemed "poor".

Figure 8 is a comparisons between experimental, numerical, and correlation logarithmic decrements for both force and wave amplitude decay methods for water. The experimental and numerical logarithmic decrements were time averaged. Figure 9 is similar to Figure 8 except the working fluid is LN2. Most wave amplitude decay results were left out of the LN2 plot because the decay rate was close to 0 and the dominant mode excited was not the first lateral slosh mode in about half of the tests, both of which reduce the accuracy of taking fluid height measurements. Data exhibiting a rotational mode are excluded. This was accomplished by either truncating the data used to calculate a logarithmic decrement to before rotation began or by simply excluding the entire case. The reason the rotational mode data was excluded is explained in Section V.B.5, which also includes many other general conclusions from the damping portion of this project.

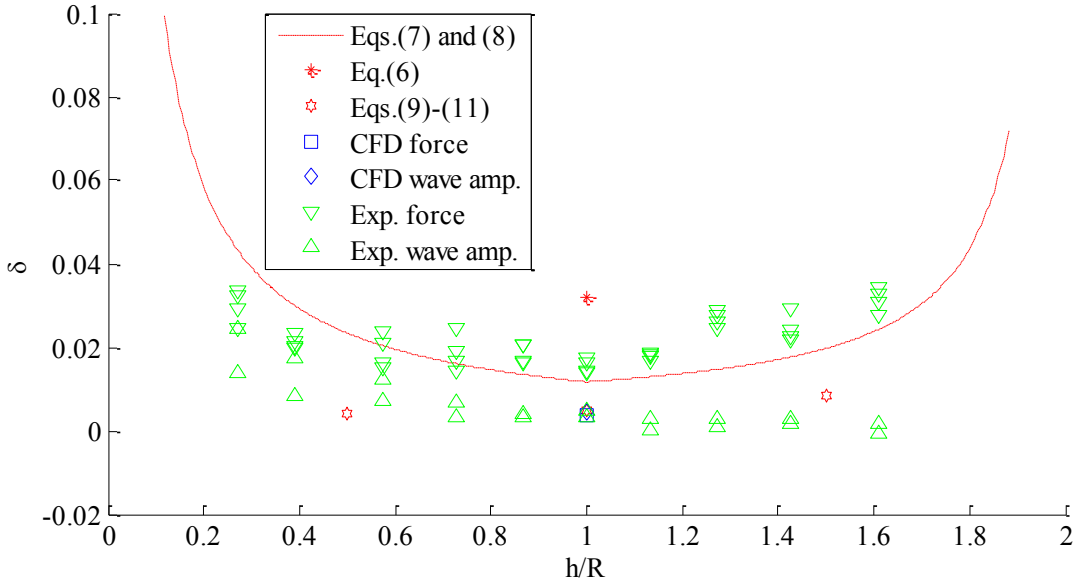

Figure 8. Logarithmic Decrement Results - Water.

Note: The cluster around h/R=1 contains the following points: one CFD force, one CFD wave amplitude, two Experimental wave amplitude, and Eq. (10) correlation.

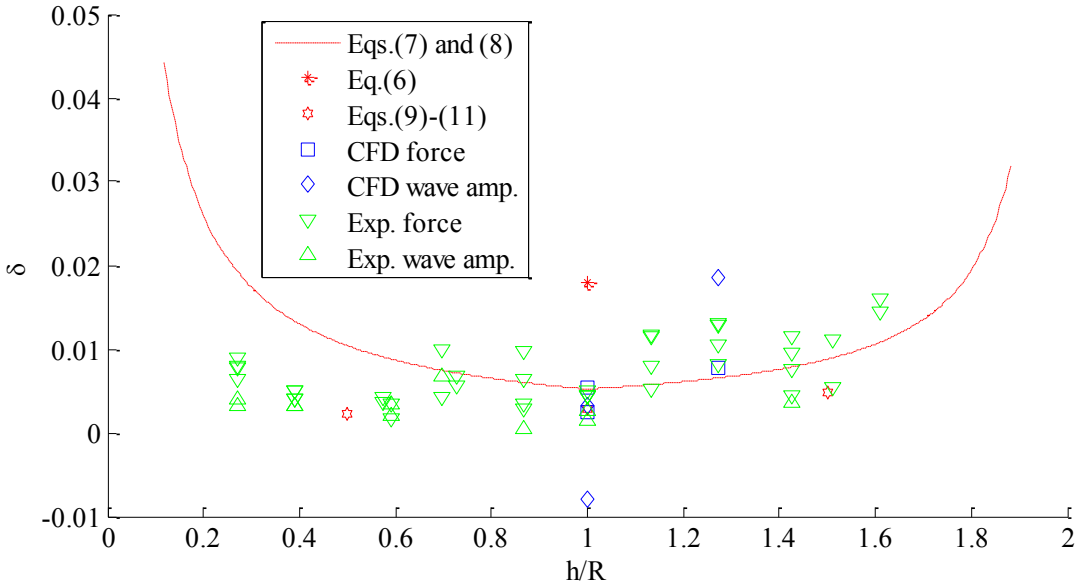

Figure 9. Logarithmic Decrement Results - LN2.

Note: The cluster around h/R=1 contains the following points: two CFD force, one CFD wave amplitude, four Experimental force, two Experimental wave amplitude, and Eq. (10) correlation.

For Figure 8, all experimental force-derived logarithmic decrements (FDLDs) fall within the previously defined "fair" agreement definition. Similar trends to those discussed for Figure 7 are present: The FDLDs are generally lower at low fill fractions and higher at high fill fractions, but with upward trends at the lowest and highest fill fractions. The Eqs. (7) and (8) correlation underpredicts damping at fill fractions greater than or equal to one and has mixed performance for fill fractions less than 1. The Eqs. (9)-(11) correlations underpredict the results, while the Eq. (6) correlation overpredicts. A local maximum at 70% volume fraction is present, which is near the location of one of the local maxima seen in Figure 7. For Figure 8, the experimental wave amplitude-derived logarithmic decrements (WADLDs) had generally "poor" agreement with the Eqs. (7) and (8) correlation, though fair to good agreement with the Eqs. (9)-(11) correlations. WADLDs were equal to or less than the FDLDs for all fill fractions. The WADLDs curve shape is different than the FDLDs. While the slight upward trend towards the lowest fill fractions is present in both, the WADLDs show a downward trend towards 0 at higher fill fractions. The reason for the downward trend is unknown, though the following discussion attempts an explanation. For the same fill fraction, lower wave amplitude damping implies that the wave height does not decrease as rapidly in time as the force. This in turn implies that the wave motion is not being attenuated as much as expected. One possible reason is low energy (low force) waves/ripples caused by the rolling waves from the upper, backwards slanted walls, in turn causing large errors for the first mode wave amplitude measurements.

Figure 8's CFD FDLD point is in good agreement with the Eq. (1110) correlation point, the CFD WADLD point, and two experimental WADLD points. The Eqs. (6)-(8) correlations over predicted the CFD FDLD and WADLD.

For fill fractions greater than 1, Figure 9 experimental FDLDs have similar comparisons and trends as those of Figure 8. However, for fill fractions less than about 0.7 (30% volume fraction), there is poor agreement with the Eqs. (7) and (8) correlation. The general trend of lower damping at low fill fractions and higher damping at high fill fractions seen in both Figure 7 and 8 can is present in Figure 9. The points corresponding to the Eqs. (9)-(11) correlations seem to have fair agreement with an interpolated FDLD curve, while the Eq. (6) correlation overpredicts. There are not enough experimental WADLD points in Figure 9 to define a trend for fill fractions greater than 1. For fill fractions less or equal to 1, the WADLDs are close to 0. An interpolated WADLD curve seems to show fair agreement with Eq. (9) correlation. There is good agreement with the Eq. (1110) correlation point, while the Eqs. (7) and (8) correlation tends to overpredict wave amplitude damping. For a fill fraction of 1, Figure 9's two CFD FDLD points have fair-to-good agreement with the Eq. (1110) correlation point, the Eqs. (7) and (8) correlation, the experimental FDLDs, experimental WADLDs, and one CFD WADLD. For the 70% volume fraction case, there is fair agreement with the Eqs. (7) and (8) correlation and the average experimental FDLDs. Two of the CFD WADLDs had poor agreement, one of which was calculated to be negative. The high error for the CFD WADLDs is from spikes in the wave height versus time plots, which come from splashing and higher order modes.

Note that both Figure 8 and Figure ***9*** contain logarithmic decrement results from tests that heavily excited modes other than the first lateral slosh mode; this likely accounts for the majority of the variation between repeated tests. The logarithmic decrements for LN2 are lower than for water, which makes physical sense because the kinematic viscosity of LN2 is about five times lower than water, and lower viscosity fluids experience less damping[12]. More general conclusions from the damping portion of this project are discussed in Section V.B.5.

An interesting outcome of the damping simulations was that force amplitude was approximately two times higher than the experimental results. Despite that, the CFD FDLDs had fair-to-good agreement with the experimental FDLDs. Some of the poor CFD force and wave amplitude agreement can probably be attributed to the coarse mesh. However, a single damping simulation was repeated with a 1.3M cell mesh, and the forces agreed well with the coarser mesh case (results from this simulation are not presented in this paper). This implies that there may be an experiment design flaw in the damping tests that is resulting in a measured force amplitude that is too small. One hypothesis for this is as follows: The rail static friction provides a structural path to the force sensor in parallel with the main connection to the force sensor. The structural path can be thought of as a spring with a high spring constant, and the minute deflection of the frame and force sensor could be causing some of the force to be taken up by the structural path "spring", thus reducing the measured force significantly. This would not affect the logarithmic decrement because changes in force are what is important for that calculation, not absolute force. This hypothesis will be tested next year by repeating the damping tests using the floating tank setup.

4. *Qualitative Surface Comparisons*

Figure 10 Figure 11 compare images and CFD frames at various times for two of the damping tests. The view point is from the top looking down, with forcing to the left and right. Exact lighting, surface features, and perspective could not be reproduced in STAR-CCM+. For damping tests, the camera was tilted a few degrees towards the ruler to bring more of the upper part of the ruler into view. The error on time stamps is +/- 25 ms, most of which is from the CFD frames and images being taken at different frame rates. Fluid, excitation frequency, excitation amplitude, and volume fraction are given in the figure captions.

Overall qualtiative comparison quality is difficult to rate. Many features are hard to identify due to top-down perspective, particularly in the experiment images. Side views are better for seeing the mode shapes, but the metallic tank precluded that perspective. Examining the reflections and shadows carefully, one can make out most of the primary features in an experiment image and CFD frame pair. Wave breakup and droplets are not accurately modelled in the CFD due to neglecting surface tension and having a coarse (relative to droplet size) mesh. Small surface ripples are obscured by LN2 boiling. As mentioned in Section III.B.3, image correction for the fisheye lens was attempted, but did not seem to produce a significant improvement. The primary viewpoint difference is not caused by warping from the fisheye lense, but from the limited field of view and perspective in STAR-CCM+. It was not possible to have the STAR-CCM+ camera at the same location as the experimental camera and still see the fluid surface edges.

A few specific features are worth pointing out. In Figure 11.b and f, c and g, and d and h, spouts near the center of the images are visible. Figure 11.d and h exhibit asymmetry despite symmetric initial conditions due to significant splashing and wave breakup. Figure 11.d shows a wave breakup in the bottom left of the image, but not the top left. While may be difficult to see, Figure 11.h exhibits a similar feature as evidenced by the spike and crests along the bottom left of the frame, though the breakup is less pronounced due to the aforementioned reasons.

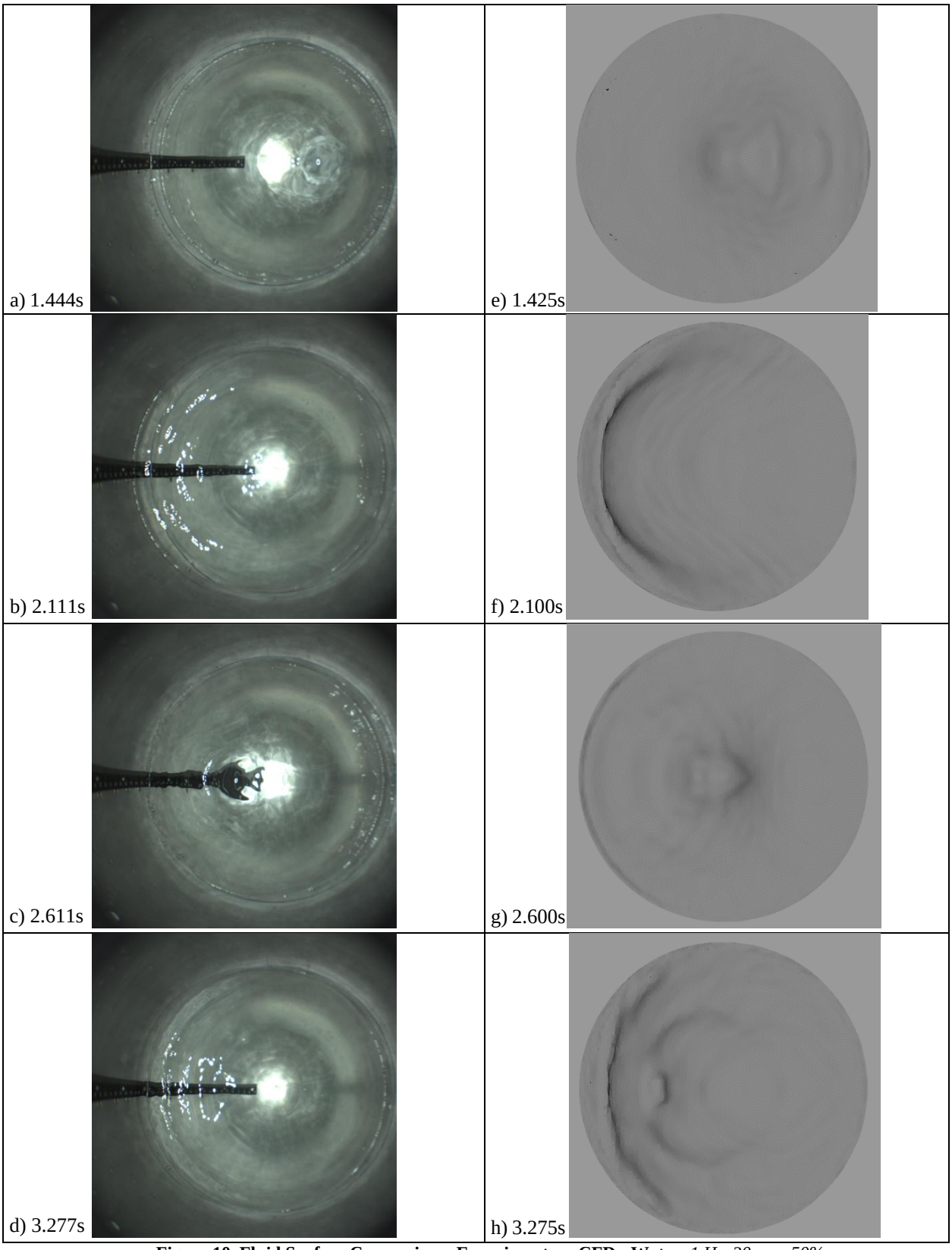

Figure 10. Fluid Surface Comparison: Experiment vs. CFD - Water. *1 Hz, 30 mm, 50%*

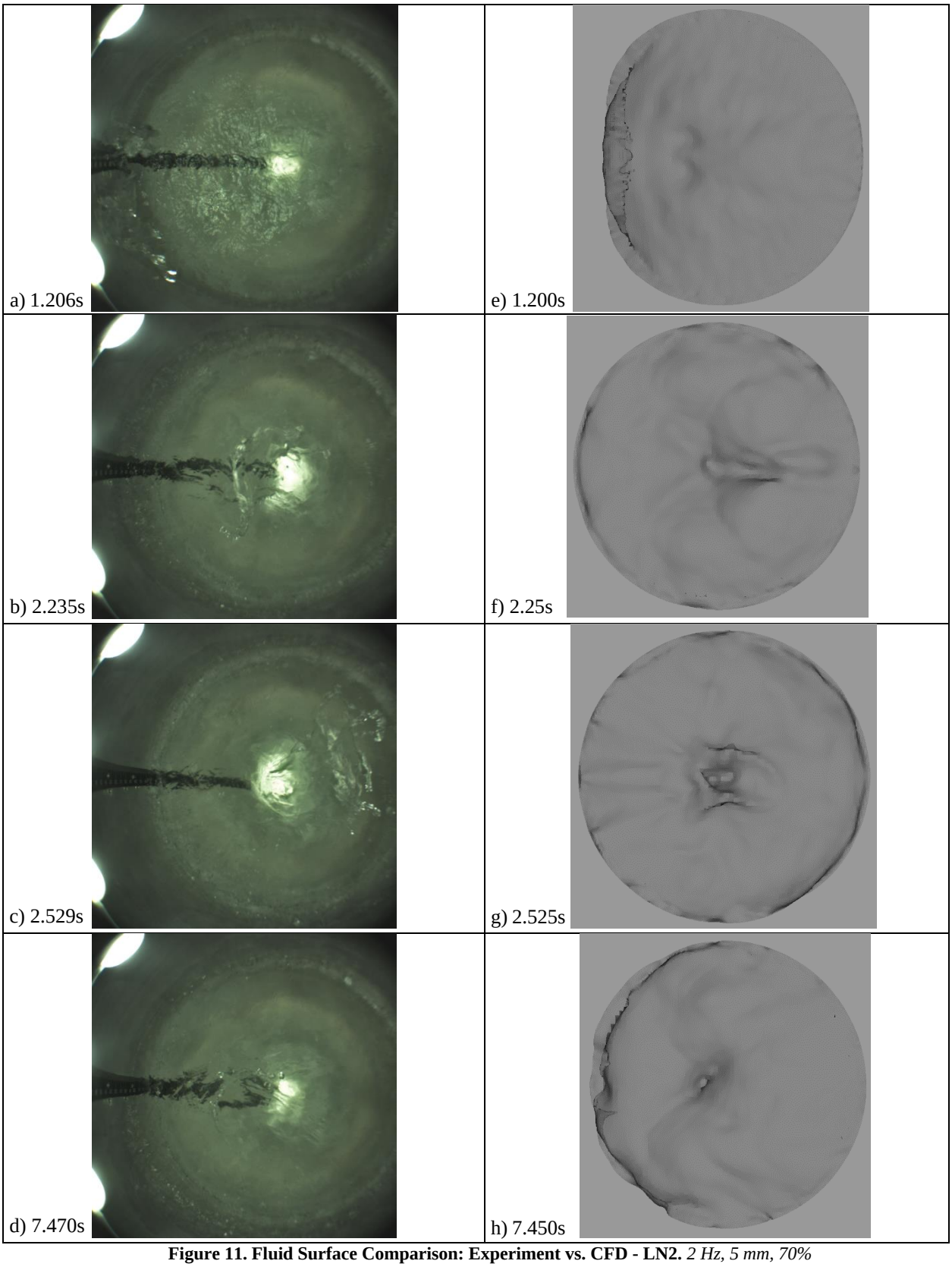

Figure 11. Fluid Surface Comparison: Experiment vs. CFD - LN2. *2 Hz, 5 mm, 70%*

5. *Further Discussion of Results*

Of the two methods, force decay and wave amplitude decay, force decay resulted in less variable logarithmic decrements and was therefore likely more accurate. Physically, this makes sense. Surface waves with small slosh mass but high amplitude will be present as spikes in wave height versus time plots but will not be as apparent in force versus time plots. The force decay gives a better sense of the decay of the momentum and energy of the flow, which is ultimately the point of the damping factor.

Splashing was observed for many cases, which resulted in a rapid decay of force and wave height corresponding to a decrease in logarithmic decrement from a large value until the wave breaking stopped. After the wave breaking stopped, if no other modes had been excited, the first lateral slosh mode would decay roughly exponentially resulting in a roughly constant logarithmic decrement. As time increased and the wave height became small, the force-derived logarithmic decrement tended to increase slightly due to a roughly linear decay in force. The signal to noise ratio became too poor for valley to peak force amplitudes of 0.4 N or less, so the force data was truncated there. The logarithmic decrements presented above were time averages of these curves.

A swirling mode was observed during some tests that had a much longer decay than the lateral mode, resulting in a logarithmic decrement near zero. A rotational mode was excited more often by the 2 Hz excitation than the 1 Hz excitation, and usually only after splashing had occurred. The theory for splashing-induced rotation is as follows: The chaotic motion from a breaking wave re-entering the bulk fluid causes an off-axis force and resulting fluid motion. A component of the splash-induced motion is re-directed by the wall giving an initial rotation. Since the rotational slosh mode in spherical tanks is less damped than the lateral slosh mode (observed in these experiments), and the rotational slosh first mode frequency is near that of the lateral slosh first mode[2], the lateral sloshing mode tends to transfer energy to the rotational mode and decay quickly.

It is clear from the images and force data that other modes besides the first lateral mode can have significant energy and that the majority of the data was taken in the nonlinear slosh regime. This is likely caused by forcing at frequencies not equal to the first lateral mode frequency, as well as splashing. The other types of modes strongly excited by some of these tests included: the second lateral mode, the first rotational mode, off-axis first lateral mode, symmetric modes, chaotic motion, and various combinations. Having strongly excited modes other than the first lateral mode made force and wall height measurements very "noisy" for calculating the logarithmic decrement for the first lateral mode and made the results unreliable. The wide variety of slosh modes that can be excited from a lateral excitation casts doubt on the usefulness of simple characterizing parameters, e.g. damping factor, for large amplitude/nonlinear slosh. It may be that only meaningful ways to characterize damping for these motions are with simulations or experiments.

Before testing, it was reasoned that damping factor should be independent of excitation frequency and amplitude, so the values for each were somewhat arbitrarily chosen. Further research into damping in spherical tanks[12] showed that there may be some dependence on excitation frequency. Specifically, the damping factor's dependence on frequency increased with decreasing tank diameter and increasing fluid viscosity, i.e. as the tank gets smaller and the viscosity increases, the effect of frequency on the damping factor increases. Ref. 12 showed no dependence on excitation amplitude. However, future work by the same group[13] showed a dependence of damping factor on excitation amplitude, the data for which is presented in Figure 7. Thus, some of the variation at each fill fraction seen in Figure 8 and Figure ***9*** may be caused by the fact that the tank was excited at two different frequency/amplitude combinations.

Judging from the results presented in Figure 7Figure ***9*** and the discussions above, either there are extensive, large experimental errors, the correlations are not applicable, or the correlations are inadequate; most likely it is a combination of all three. The correlations do not consider excitation amplitude nor excitation frequency despite clear evidence that such dependencies exist. It is possible that the high nonlinearity of the slosh in these tests invalidates the use of these correlations. Even though the redefined "fair" was used to describe much of the results' comparisons to the correlations, 100% error is probably unacceptable for making engineering decisions. Clearly, more research needs to be done to set amplitude, frequency, diameter, etc. ranges of applicability for the correlations and to create new correlations that are valid over larger ranges of the relevant parameters.

Ref. 12 damping tests were done by exciting motion until a maximum wave height was reached, then stopping motion. The damping tests presented in this paper had varying maximum wave height because a fixed number of excitation cycles (two) was used. Future damping tests will excite the fluid with a constant, low amplitude oscillation at the first mode resonant frequency until a maximum wave height is achieved (pre-wave break). Then the motion will be stopped, and data will be recorded while the slosh motion decays. This should eliminate the possible error introduced by dependence on excitation frequency and wave height. It should also minimize energy input into modes other than the first lateral mode.

C. Forced Excitation

1. *Time Domain Plots*

The following three figures are plots of experimental, analytical, and numerical and force in the excitation direction versus time. These three cases were chosen because they were the ones simulated in CFD. Each plot caption lists the forcing frequency, actual position amplitude, and volume fraction.

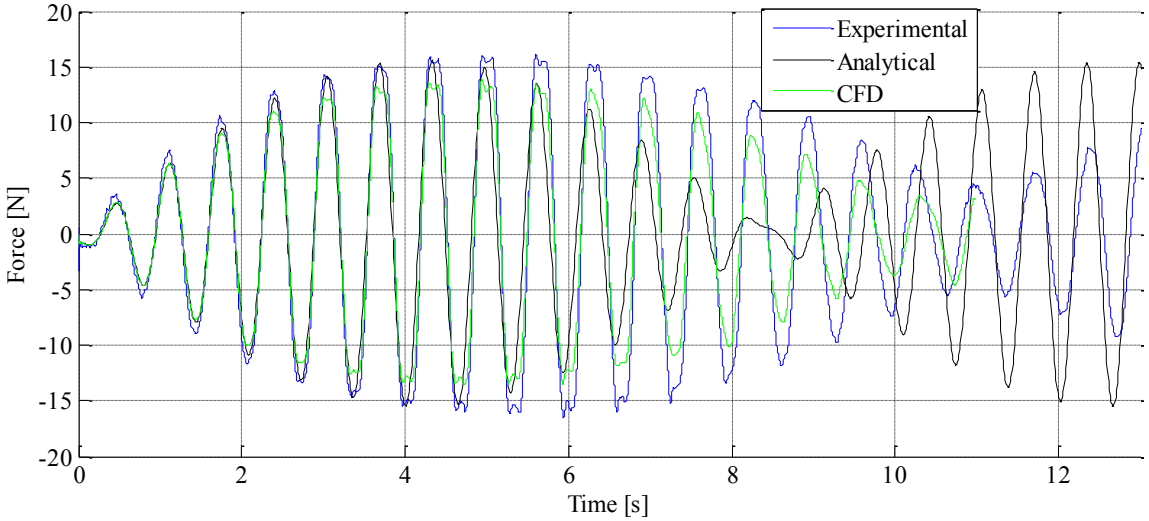

Figure 12. Water Slosh Force vs. Time Comparison. *1.5 Hz, 3.04 mm, 50%*

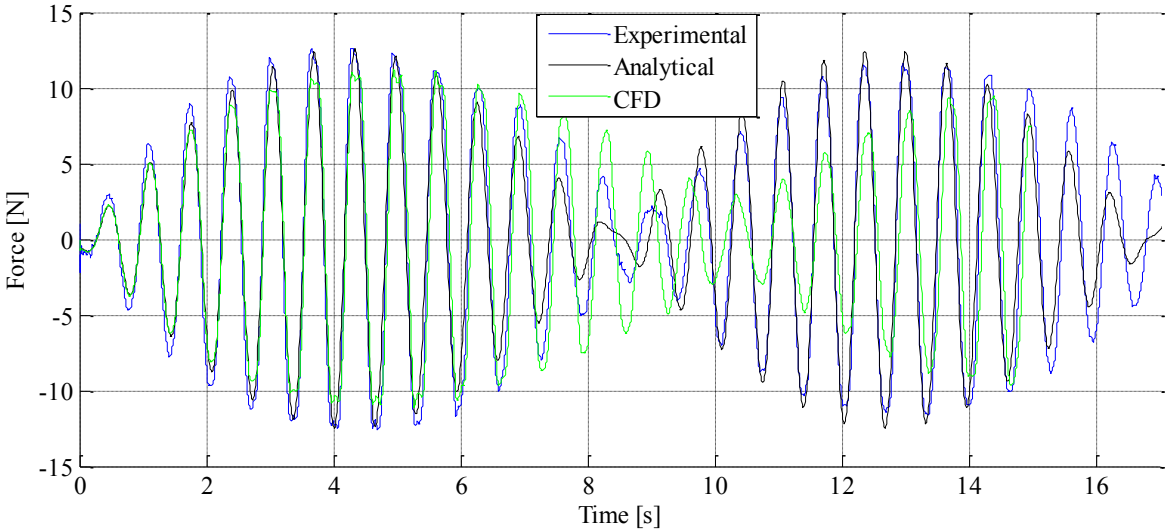

Figure 13. LN2 Slosh Force vs. Time Comparison. *1.5 Hz, 3.04 mm, 50%*

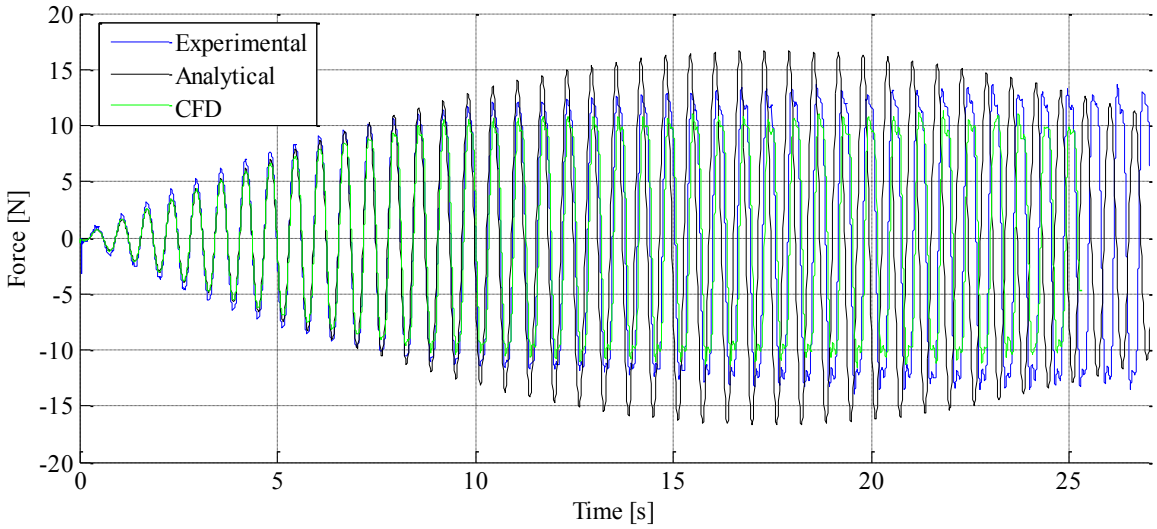

Figure 14. LN2 Slosh Force vs. Time Comparison. *1.59 Hz, 0.93 mm, 50%*

The CFD peak force amplitude is consistently low by about 15%. This is mostly likely due to the low cell-count mesh, which was determined to be insufficient for mesh independence. The modelling assumptions used to derive the analytical force equations probably account for the majority of the analytical error seen in the above figures. Also, the analytical force was determined to be very sensitive to fluid volume; fluid volume measurement was identified as a signifcant source of experimental error. In Figure 14, the forcing frequency is about 0.03 Hz below the theoretical resonant frequency; the reason for this frequency was chosen is discussed in the next section. The analytical force grows unbounded when calculated with the theoretical resonant frequency. The analytical waveform in Figure 14 becomes more and more out of phase from the CFD and experimental waveforms as time progresses, despite the forcing frequencies for all three waveforms being identical. This is again due to the forcing frequency being just below the analytical resonant frequency. In Figure 12, the period of the long term pulsing mode seems to be predicted well by the CFD, but the CFD underpredicts the period by about 2 s for LN2 in Figure 13.

The following three figures are plots of experimental, analytical, and numerical wave height. For water, experimental wave heights are shown as maximum and minimum points. Experimental wave height for LN2 is unavailable due to the light source failing during testing (see Section III.D.2). The gaps in the numerical data in Figure 17 were due to errors in tabular output from the CFD program.

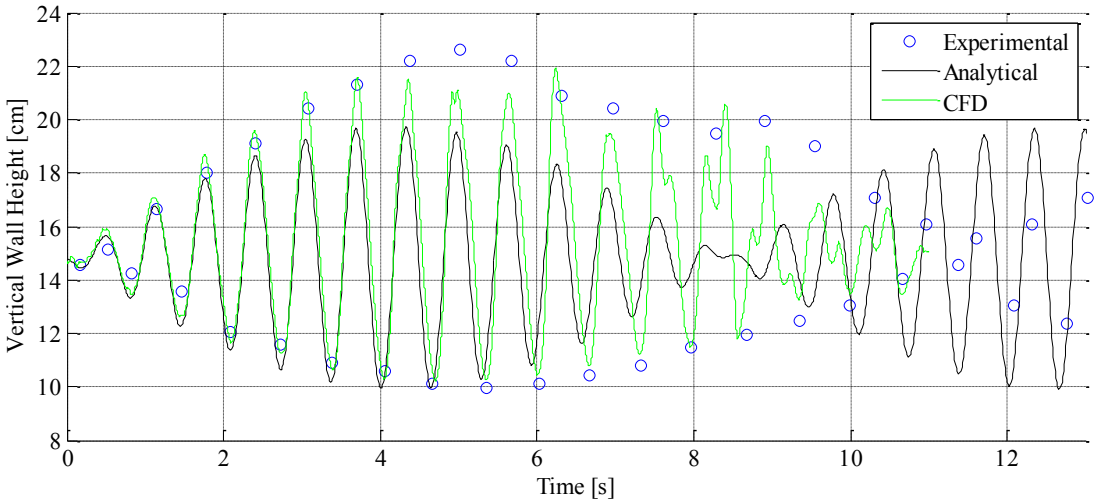

Figure 15. Water Slosh Wave Height vs. Time Comparison. *1.5 Hz, 3.04 mm, 50%*

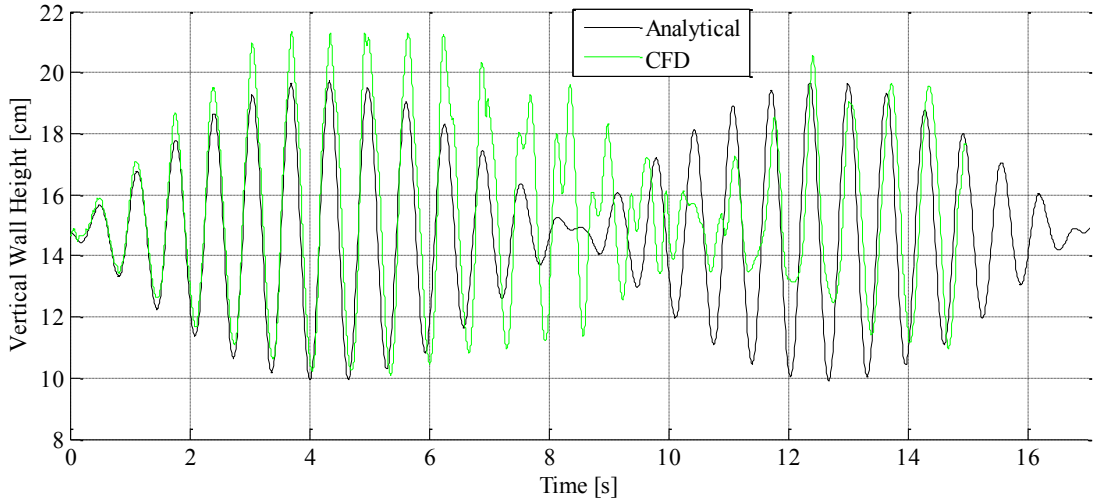

Figure 16. LN2 Slosh Wave Height vs. Time Comparison. *1.5 Hz, 3.04 mm, 50%*

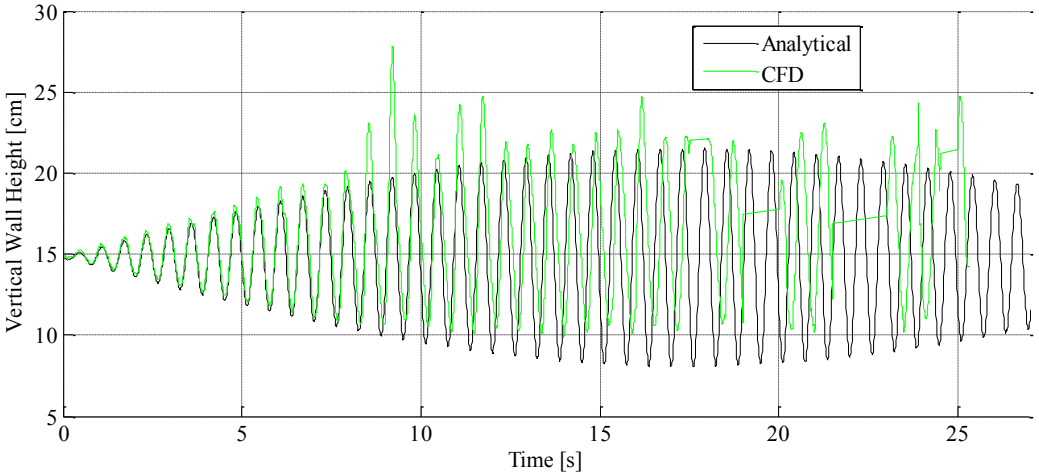

Figure 17. LN2 Slosh Wave Height vs. Time Comparison. *1.59 Hz, 0.93 mm, 50%*

Wall height comparisons did not agree as well as the force comparisons. For Figure 15, the peak amplitude error for most points is less than 20%. Splashing can be seen as spikes and split peaks in the CFD curves. Similar to the force versus time plots, a discrepancy between the analytical and CFD frequency of the long term pulsing mode of the 1.5 Hz cases is apparent. This is most likely due volume sensitity of the analytical solution mentioned earlier. The unbounded growth discussion and out-of-phase comments for Figure 14 also apply to Figure 17. Additonal time series plots have not been included for sake of brevity.

2. *Other Plots*

The following two plots are of the nondimensional force parameter versus the nondimensional frequency parameter. Note that no averaging across repeated tests was done; many points overlap almost perfectly.

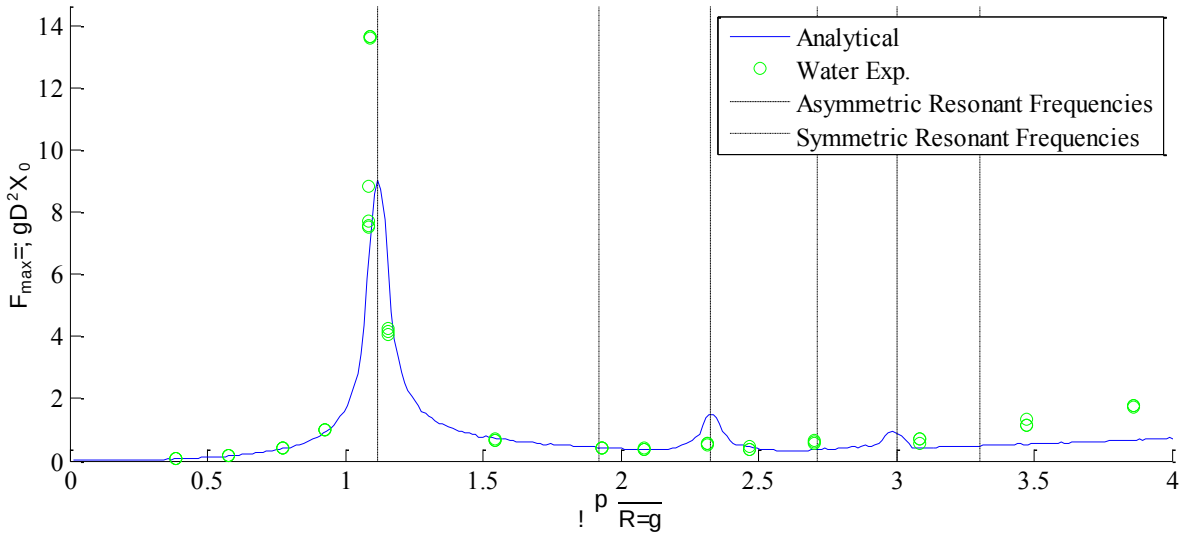

Figure 18. Force Parameter vs. Frequency Parameter for Water, 20% Volume Fraction.

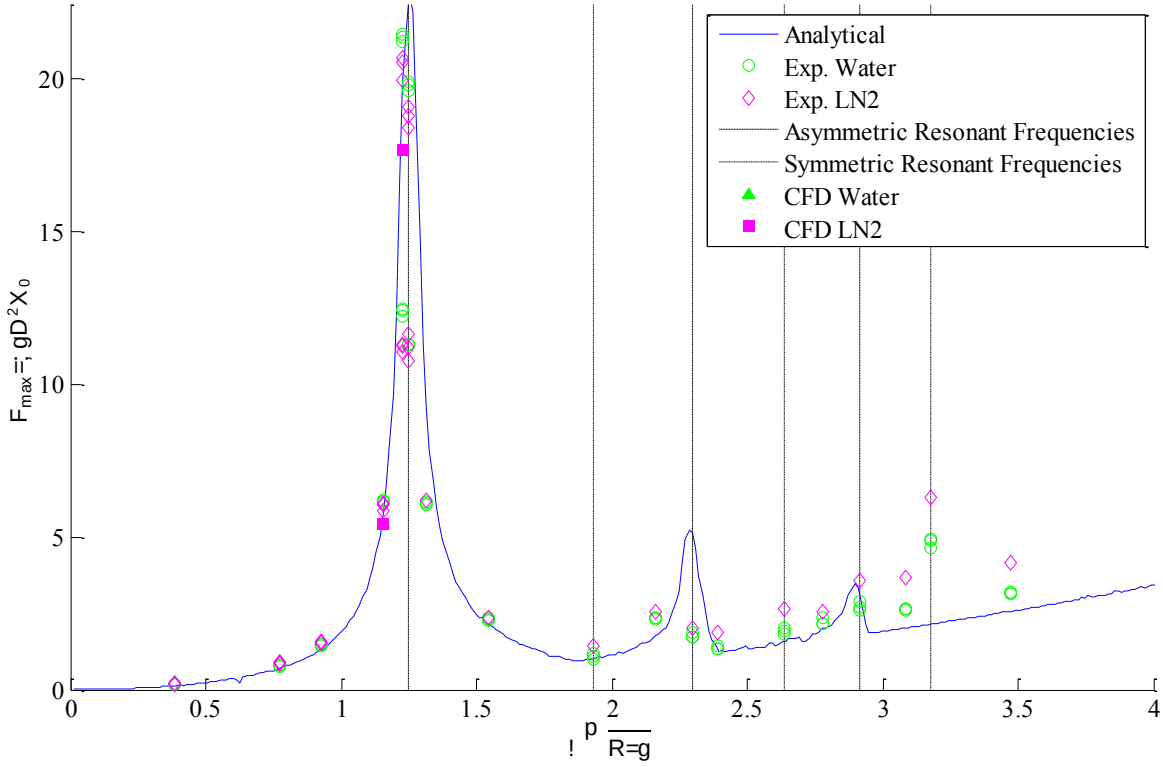

Figure 19. Force Parameter vs. Frequency Parameter for Water and LN2, 50% Volume Fraction.

As can be seen, there is generally good agreement between the analytical, experimental, and numerical results, though the agreement lessens for frequencies around and above the second asymmetric mode frequency. The poor agreement for higher frequencies is likely the result of the signicant splashing and chaotic sloshing observed at those frequencies, as well as analytical model assumption error. The second and third asymmetric modes were not successfully directly* excited by any test. Oddly, the third symmetric mode seems to have been directly excited, even

* "directly" meaning forced at that frequency and have that mode become dominant. Of course all modes are always present with differing amounts of energy.

in repeated tests, for the 50% volume fraction cases. Examining the images of the water tests for that excitation frequency shows a symmetric mode forming near the end of the 30 s tests, though the top-view perspective makes identifying the mode shape difficult. Note that if the tests became rotational, the data was truncated in post-processing at that point to prevent the usually larger amplitude rotational modes from affecting the force parameter calculations.

The cluster of points near the theoretical first mode frequency in the middle of the analytical spike in Figure 19 are from the higher amplitude (1.849 mm), 1.59 Hz and 1.618 Hz (theoretical first mode resonance) test cases. The lower amplitude (0.926 mm) cases at the same frequencies can be seen further up the analytical spike, with the 1.59 Hz case having the highest force. The reason the higher amplitude cases' force parameters are lower than lower amplitude cases' force parameters is that the force parameter has a X_0 in the denominator and the force gain due to amplitude was marginal. One explanation for the slightly-lower-than-predicted first mode frequency is inaccuracies from interpolating points read from the theory plot instead of doing calculations. However, tabulated points from Ref. 3 were included in the interpolation; the error due to this method cannot account for the difference. Other possible explanations for the difference between theoretical first mode resonant frequency and the frequency that resulted in the largest force include the tank not being perfectly spherical and forcing at too large of an amplitude, which resulted in premature wave breaking at the theoretical resonant frequency.

In Figure 19, the LN2 force parameter was consistently higher than the water force parameter for frequency parameters approximately equal to 2 and greater. The only possible explanation is that, since the force parameter is inversely proportional to density and the density of LN2 is lower than water, the forces were not proportionally lower for LN2 than water. However, why the force was not proportionally lower for LN2 is unknown. The opposite trend is apparent for frequencies around the first mode frequency.

Figure 20 shows an alternative nondimensional force parameter versus fill fraction and $\frac{X_0}{D}$. This force parameter is not the same as the one shown in Figure 2, Figure 18, and Figure 19. This one is calculated using the maximum slosh force measured for any excitation frequency for a given fill fraction, which in these experiments occured just below the theoretical resonant frequency. Also note that the X_0 in the denominator of the previous force parameter's definition is replaced by another D. The data lines in Figure 20 are from tests involving a 32 in diameter tank with water[13]. Five of the other six points are from experiments performed for this project; the maximum forces and excitation amplitudes were averaged across repeated tests to yield these points (variation was low). The sixth point is from a LN2 simulation at the same frequency that resulted in a maximum force in the 50% volume fraction LN2 experiments.

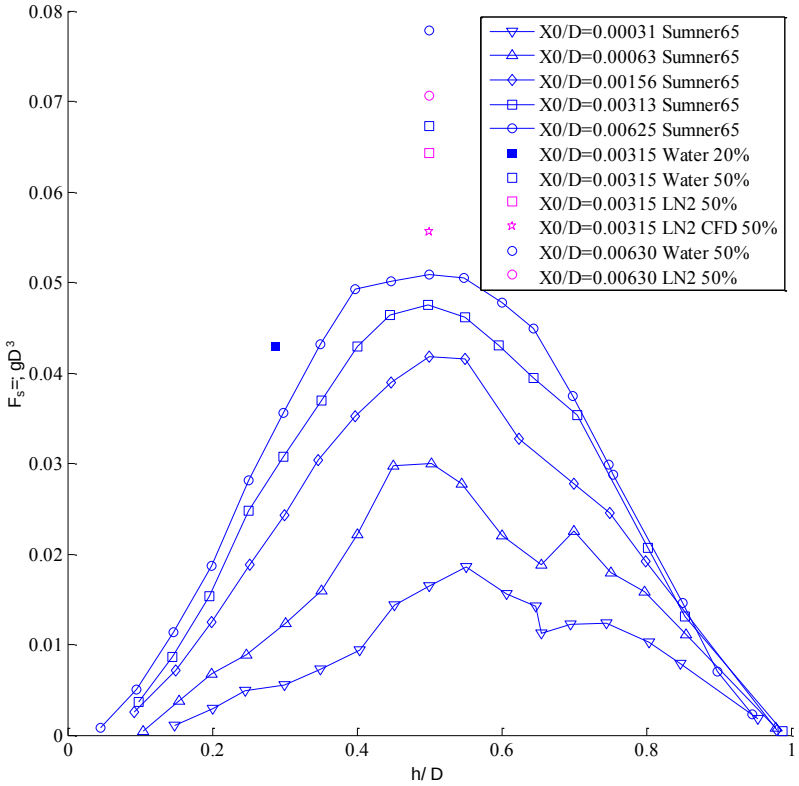

Figure 20. Force Parameter vs. Fill Fraction vs. Amplitude.

Maximum slosh force is clearly dependent on both fill fraction and excitation amplitude, both of which make physical sense. The D^3 term in the denominator of this force parameter is likely the reason the Ref. 13 results are lower than the results from this project. Another observation from Figure 19 and Figure 20 is that LN2 maximum slosh forces are smaller than water slosh forces, which is likely due to the lower density of LN2.

3. *Other Interesting Results*

Rotation/swirl were common at frequencies equal to and above the first mode natural frequency. While exciting near or at the theoretical first mode frequency, after the initial build up and wave break, the force tended to decrease in time to a point, then begin increasing due to rotation until a rotational mode with larger wave and force amplitude than the lateral mode developed. After some time, this mode began decaying into an off-axis lateral slosh mode. This would turn back into the rotational mode, and the pattern would continue. The off-axis angle and rotation direction seemed to be very sensitive to initial conditions and frequency. The speed at which these patterns developed and decayed was dependent on amplitude, with higher amplitudes causing faster evolution. The first rotational mode resonant frequency was determined by accident to be approximately 1.7 Hz at 50% fill level with water. It was excited in one test when the test was started with a small amount of residual rotation from a previous run. The *highest* force from any test during the project was recorded during that test.

Also interesting is the fact that some of the *lowest* forces were recorded for 1.7 Hz excitation and 50% fill if the fluid (either water or LN2) did not start rotating. This is apparent in Figure 19; the first set of data points after the first asymmetric mode line correspond to 1.7 Hz excitation and are signifcantly lower than the analytical prediction. If the fluid was allowed to become very still before starting, rotation would not develop in tests run for 90 s. The peak measured total force for those tests was more than two times smaller than the peak fluid force, as calculated by subtracting an empty tank run from the total force, implying that the fluid motion was almost perfectly out of phase with the excitation. Examination of the images support this conclusion. The fact that the peak force sensor readings more than doubled when the excitation stopped also supports this conclusion. Note there is a similar feature present in Figure 18, but the difference between that cluster of points and the analytical solution is not as extreme and the frequency is lower at 1.5 Hz. The out of phase behavior was not as apparent for that case, but fine tuning the frequency would probably yield a similar result to that for the 50% volume fraction case.

High excitation frequency (3 Hz and higher) cases usually exhibited chaotic motion, usually with a swirling component. Wave patterns can sometimes be seen in the images, but no attempts to classify these have been made.

Images of forced sinusoidal testing have not been included for sake of brevity and due to the lack of LN2 images because of the failed light source. The comparison between water images and the CFD fluid surface for forced sinusoidal tests was similar to the corresponding comparison from the damping tests.

VI. Final Conclusions and Future Work

To reiterate, the overall goal of this project is to perform slosh experiments to collect data relevant to in-space cryogenic propellant storage, management, and transfer applications, and to validate CFD models using that data. Progress towards this goal has been made, though much work still needs to be done. Despite the infancy of this project, a few overall conclusions and future work recommendations can be made.

There is some confidence in the CFD models used in this project to accurately predict fluid slosh. The errors are mostly likely due to a low cell-count mesh. Many more damping and forced excitation simulations will be run, likely in batches on NASA servers. Simulations of the new experimental setups discussed below will also be run.

An uncertainty analysis needs to be performed to determine the number of repeated tests required for damping and force excitation tests, and to determine overall uncertainties in the experimental results.

Various hardware and software improvements to the current test setups will be made, including frame stiffening, motion controller tuning, new lighting, a new fluid height measurement technique, and improved thermocouple-related instrumentation.

The damping tests need to be re-done with a focus on not strongly exciting modes other than the first lateral mode. Attempts may also be made to separate the linear and nonlinear slosh cases in the new damping tests. Both of these should reduce the variance seen in the logarithmic decrements. The new sets of damping data will be compared to the correlations to attempt to set applicability ranges.

Forced excitation tests at more fill fractions will be run. After the new damping and forced excitation tests with both water and LN2 are completed, the significance of further water testing will be examined. The purpose of the water tests were to validate the experimental setup. Water slosh has been extensively studied in the past, and the current water tests seem to be in fair agreement with past results. If the new round of testing yields better agreement, repeating every LN2 test with water will not generate much new, useful information.

In addition to improvements to the current test setups, new ground-based tests are being planned. The tank frame was designed to allow for the easy addition of a free, rotational, pitching axis perpendicular to the linear motion axis. This is accomplished by a narrowing of the tank subframe and the addition of two pillow block bearings and axles. Fluid management device, e.g. baffles, may be incorporated in some tests.

The "floating tank" test setup has several significant advantages over current state-of-the-art ground-based slosh test setups like hanging pendulums and linear rails. As discussed earlier, linear rail test setups suffer from static and kinetic nonlinear friction. Hanging pendulum test setups have less friction, but they are limited to small amplitudes to prevent vertical motion and are often multiple stories tall. Floating a tank on air pucks on a flat floor allows for free 3 DOF movement (two translation + yaw). With the addition of a propulsion module, spacecraft dynamics under the influence of fluid slosh can be experimentally simulated on the ground. The floating tank approach is also easily scalable to large tanks; the relatively small air pucks shown in Figure 4 can each support 250 lbs. Future work may include multi-free-DOF motion tests using this approach.

To fulfill the "in-space" portion of the goal, microgravity experiments and simulations need to be performed. Parabolic flight tests are being planned for next year. Parabolic flight hardware will include the same tank, main frame, and subframe, but instead of being fixed to the linear motion table, it will be mounted to an aircraft. The tank will be fixed relative to the aircraft; no free DOFs will be tested on the aircraft for safety concerns. Similar instrumentation will be used.

For large amplitude slosh, the first lateral mode may not be the strongest one excited. Of the additional modes that can be excited, rotational modes seem to be particularly important in terms of amplitude and long decay times. More research needs into non-lateral slosh needs to be done, though none is planned by the authors at this time.

A final goal is to compile all test and simulation data from this project in the LSP Electronic Slosh Data Catalog (ESCD) by Summer 2016 so that it will be available to all NASA and NASA-affiliated slosh researchers.

Acknowledgments

The authors would like to acknowledge and thank the following entities for the invaluable assistance that they have provided in the success of this project to date: NASA Launch Services Program for guidance and support of the project (including mentoring and providing the basis in past work on slosh behavior), the FIT machine shop for their assistance in fabricating the test article, colleagues in the FIT ASAP and Mechatronics labs for their assistance and encouragement in this project. Additionally, the authors wish to thank the contributions of Bernard Kutter of ULA for his suggestions of tank material flight applicability for the effort, and Dr. Barry Battista of Tech Masters for his assistance, suggestions, and guidance in various aspects of mounting instrumentation to the tank.

VII. References

[1]CD-Adapco, STAR-CCM+, Ver. 9.04, software package, 2014.

[2]Ibrahim, R., *Liquid Sloshing Dynamics Theory and Applications*, Cambridge University Press, New York, 2005.

[3]McIver, P., "Sloshing Frequencies for Cylindrical and Spherical Containers Filled to an Arbitrary Depth", *Journal of Fluid Mechanics*, Vol. 201, 1989, pp. 243-257.

[4]Budiansky, B., "Sloshing of Liquids in Circular Canals and Spherical Tanks", Lockheed Aircraft Corporation, 1958.

[5]The MathWorks, Inc., MATLAB Release 2014a, software package, Natick, Massachusetts.

[6]Zhou, R. et al., "Experimental and Numerical Investagtion of Liquid Slosh Behavior Using Ground-Based Platforms", *Journal of Spacecraft and Rockets*, Vol. 49, No. 6, 2012, pp. 1194-1204.

[7]National Instruments, LabVIEW 2012, software package.

[8]Beckhoff Automation, TwinCAT 3, software package, 2015.

[9]NASA, GFSSP, Ver. 6.05, software package, 2015.

[10]Abramson, N. H., *The Dynamic Behavior of Liquids in Moving Containers*, NASA SP-106, 1966.

[11]Dodge, F. T., *The New 'Dynamic Behavior Of Liquids in Moving Containers'*, SouthWest Research Institute, San Antonio, TX, 2000.

[12]Sumner, I. E., Stofan, A. J, *An Experimental Investigation of the Viscous Damping of Liquid Sloshing in Spherical Tanks*, NASA TN D-1991, 1963.

[13]Sumner, I. E., *Experimentally Determined Pendulum Analogy of Liquid Sloshing in Spherical and Oblate-Spheroidal Tanks*, NASA TN D-2737, 1965.